Aerospace Science and Technology, Volume 101, June 2020, Article number 105846
DOI:10.1016/j.ast.2020.105846

Characterization of Axial Compressor Performance at Locked Rotor and Torque-free Windmill Conditions

Luis E. Ferrer-Vidal *, Alejandro Iglesias-Pérez, Vassilios Pachidis

Cranfield University, Cranfield, Bedforshire, MK43 0AL, United Kingdom

ARTICLE INFO

Keywords:
Compressor
CFD
RANS
URANS
Windmilling
Sub-idle
Characteristics

ABSTRACT

Prediction of aero-engine performance in the sub-idle regime is becoming increasingly important. Performance prediction tools rely on component maps to enable system-level simulations. Methods to obtain compressor sub-idle maps have traditionally relied on low-order extrapolations, but the continued development of robust turbomachinery numerical methods suggest that these tools may be sufficiently robust to allow improved performance predictions at these challenging off-design conditions. In this work, an axial compressor rig is used to obtain locked rotor and windmill performance characteristics which are then compared against results from Computational Fluid Dynamics (CFD) simulations. This paper assesses the capability of steady state RANS CFD as a tool for the prediction of sub-idle compressor performance and helps delineate the minimal modelling fidelity required to obtain sufficiently accurate performance models. The multi-stage performance of axial compressors at locked rotor and at the zero-torque windmilling condition are discussed. Windmilling multi-stage compressors are found to operate with the front stages compressing the flow and the last stages expanding to satisfy the power balance. The torque-free windmilling behavior of axial compressors can be described non-dimensionally, allowing limited numerical simulations to be used to build sub-idle performance models.

1. Introduction

An aviation engine is exposed to the sub-idle regime on start-up or during windmill relight. While these events have historically not warranted a detailed performance evaluation, more stringent certification and customer requirements, and the push for marginal benefits in fuel efficiency have highlighted the need for accurate sub-idle performance characterization (EASA, 2015). Additionally, modern engines with increasing by-pass ratios put a strain on relight capability, while larger gearboxes and driven accessories also contribute to increased windmilling drag and reduced starting performance (Zachos, 2013). As the trend for higher by-pass ratios and geared configurations continues to increase, so too does the need for improved sub-idle performance, requiring improved prediction techniques.

In order to accurately predict whole-engine performance at sub-idle using a zero-dimensional performance solver, maps are required for the different engine components. As data in these regions is scarce, a way to generate sub-idle maps needs to be devised. Several techniques have come about for the generation of sub-idle compressor maps using a variety of graphical (Kurzke, 1996), and analytical (Agrawal and Yunis, 1982), (Gaudet and Gauthier, 2007) methods. Generally, these low-fidelity approximations limit the accuracy of the generated performance data. A review of these methods can be found in

* *Corresponding author.*
E-mail address: l.ferrer-vidal@cranfield.ac.uk

(Jones et al., 2001). Previous work at Cranfield University has looked at enhancing map generation by including interpolation from limited sub-idle data, such as locked rotor and windmilling characteristics (Zachos et al., 2011), (Ferrer-Vidal et al., 2018). While these last methods have shown promise, they require the locked rotor and windmilling characteristics to be calculated for accurate maps to be obtained.

Modelling of compressor performance at extreme off-design conditions typically requires specialized treatments (Righi et al, 2018). However, advances in turbomachinery CFD and the existence of robust commercial tools capable of handling compressor off-design conditions, offer an opportunity to broadly capture the physics present during off-design (Hu et al., 2018), (Kim et al., 2019), (Ghenaiet & Khalfallah, 2019). These methods offer an avenue to generate sub-idle maps from a limited number of CFD simulations relying on physics rather than on scaling approaches (Jones et al., 2001). Since the off-design conditions pose a challenge on the numerical method, the ability of RANS CFD to capture overall performance trends at these conditions, specifically locked rotor and torque-free windmill needs to be assessed. Such methods could then be used to inform map generation methods such as those described in (Zachos et al., 2011) and (Ferrer-Vidal et al., 2018).

Nomenclature

$\mathbf{\Delta h}$	Specific stagnation enthalpy change $[\boldsymbol{kJ/kg}]$
$\boldsymbol{itern}$	Iteration number
$\boldsymbol{k}$	Constant
$\boldsymbol{\dot{m}_{corr}}$	Corrected mass flow $[\boldsymbol{kg/s}]$
$\boldsymbol{mod}$	Modulus function
$\boldsymbol{N}$	Shaft speed $[RPM]$
$\boldsymbol{Np}$	Shaft speed as percentage of design speed [%]
$\mathbf{R}$	Rotor
$\boldsymbol{P}$	Pressure $[\boldsymbol{Pa}]$
$\boldsymbol{PR}$	Total pressure ratio
$\boldsymbol{T}$	Temperature $[\boldsymbol{K}]$
$\boldsymbol{tol}$	Tolerance on $\boldsymbol{\sigma_\tau}$ $[\boldsymbol{Nm}]$
$\boldsymbol{U}$	Blade speed $[\boldsymbol{m/s}]$
$\boldsymbol{V_{ax}}$	Axial velocity $[\boldsymbol{m/s}]$
$\boldsymbol{WrTP}$	Flow function $[\boldsymbol{lb\sqrt{K}/psia}]$
$\mathbf{\Delta}$	Change in a quantity
$\boldsymbol{\phi}$	Flow coefficient
$\boldsymbol{\psi}$	Loading coefficient
$\boldsymbol{\lambda}$	Pressure rise coefficient
$\boldsymbol{\zeta}$	Relaxation constant
$\boldsymbol{\gamma}$	Adiabatic coefficient
$\mathbf{\Pi}^*$	Normalized pressure loss
$\boldsymbol{\eta_{is}}$	Isentropic efficiency
$\boldsymbol{\sigma_\tau}$	Torque standard deviation $[\boldsymbol{Nm}]$
$\boldsymbol{\tau}$	Torque $[\boldsymbol{Nm}]$

Subscripts

ax	axial
c	Corrected and normalized
$corr$	Corrected to reference conditions
$in, 1, 2$	Compressor stations
is	Isentropic
ref	Reference conditions
tot	Stagnation conditions

1.1. Sub-idle compressor performance maps

The sub-idle portion of a map can be divided into three distinct regions depending on the sign of the work and total pressure changes. While any point with a pressure ratio above unity is considered inside the compressor operation region, the regions with a total pressure loss can be divided into stirrer and

turbine modes depending on the sign of the work input. In the stirrer mode, there is a work addition to the flow along with a pressure loss, while work extraction and pressure loss define the turbine mode. A key element of the map is the boundary between these last two regions, which corresponds to the torque-free windmilling characteristic. On this characteristic, there is no net work done on the gas and the net torque on the blading cancels out. The word net is key here, as different compressor stages may be operating under different regimes. In the absence of loads and frictional losses, the torque-free windmilling line can be reached by a compressor simply due to the incoming flow. In a real-life application, frictional losses and the presence of a turbine result in steady state windmilling operation occurring slightly below or above the torque-free windmilling line (Walsh and Fletcher, 2004). The torque-free windmilling line discussed in this work must therefore be understood to pertain solely to the compressor, and not the whole-engine windmill characteristic (Shou, 1981). At the lower extreme of the map, the locked rotor line corresponds to zero speed operation, where flow simply passes through the compressor, incurring a pressure loss and imparting torque on the shaft. These different regions are illustrated in Fig 1 along with notional sub-idle characteristics.

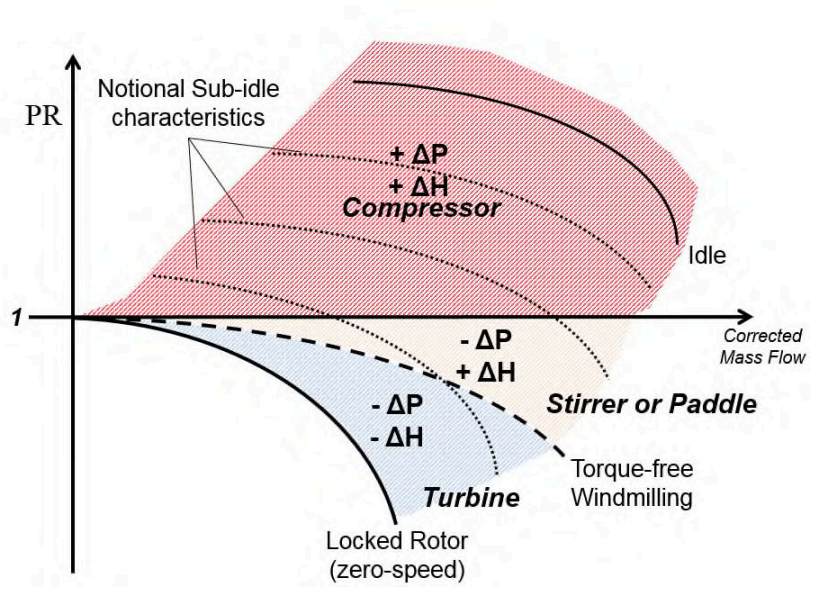

Fig. 1 – Sub-idle map regions and notional sub-idle characteristics.

Compressor maps have traditionally been represented using the parameters of corrected shaft speed, corrected mass flow, pressure ratio, and isentropic efficiency. The use of corrected quantities ensures that Mach number similarity is maintained when environmental conditions differ from standard, as this is a main driver behind compressor performance (Farokhi, 2004).

$$\dot{m}_{\mathrm{corr}} = \frac{\dot{m}\sqrt{T_{tot_1}/T_{ref}}}{\sqrt{\frac{\mathrm{P_{tot_1}}}{\mathrm{P_{ref}}}}}$$

$$N_{corr} = \frac{\mathrm{N}}{\sqrt{T_{tot}/T_{ref}}} \qquad (1)$$

$$\Pi = \frac{P_{tot_2}}{P_{tot_1}}$$

$$\eta_{is} = \frac{\Delta h_{is}}{\Delta h}$$

However, as (Riegler, 2001) explained, the use of an efficiency parameter creates issues when in the sub-idle region, since the enthalpy addition becomes zero and isentropic efficiency becomes an undetermined quantity. As explained by (Kurzke, 1996) and reviewed by (Grech, 2013), (Zachos, 2010), and (Howard, 2007), the representation of the map is not an issue as long as physical meaning is maintained. In order to bypass the difficulties mentioned above, (Riegler, 2001) and (Howard, 2007) have discussed the use of corrected shaft speed, corrected mass flow, and pressure ratio along with a torque parameter which can be defined in terms of other parameters as:

$$\frac{\tau}{\left(\frac{P_{tot_1}}{P_{ref}}\right)} = \frac{\dot{m}\sqrt{T_{tot_1}/T_{ref}}}{\sqrt{\frac{P_{tot_1}}{P_{ref}}}} \times \frac{\Delta h}{T_{tot_1}/T_{ref}} \times \left(\frac{N}{\sqrt{T_{tot_1}/T_{ref}}}\right)^2 \times \frac{60}{2\,\pi} \tag{2}$$

Using this parameter solves the definition issue at sub-idle and, along with pressure ratio and corrected mass flow, has successfully been used by (Zachos, 2010), (Grech, 2013), and (Ferrer-Vidal, 2018) to represent compressor maps down to zero speed. This torque parameter is used within this investigation in place of the isentropic efficiency. In terms of this parameter, negative torque values would correspond to turbine operation (flow imparting work on blading), with positive torques representative of the stirrer and compressor regimes (blading imparting work on flow).

2. Methods

In order to characterize compressor performance below idle, experimental data is first needed to assess the ability of RANS models to the sub-idle regime. The CFD data can then be used to extract trends regarding the locked rotor and torque-free windmilling performance for multi-stage compressors.

2.1. Sub-idle compressor rig

An experimental sub-idle rig is required to generate the sub-idle data needed for validation of the numerical approaches. The data is gathered in the form of locked rotor and windmilling characteristics, which do not require the compressor to be powered. A Rolls-Royce Allison Model 250 (M250) C20b axial compressor assembly is used. The compressor consists of 6 stages with Double Circular Arc blading (DCA) and a row of inlet guide vanes. The rig includes upstream and downstream pressure rakes for pressure ratio measurement. A venturi is positioned downstream of the compressor for mass flow measurement. A honeycomb screen and duct section ensure a uniform flow is delivered to the venturi element in accordance with ISO 5167. The compressor is unpowered, with an extraction fan and butterfly valve used to set the mass flow. The shaft is locked to obtain the locked rotor characteristic and freed to obtain the windmilling line. Data acquisition is done via a LabView virtual instrument and National Instruments data acquisition board. A filter-amplifier is used to condition the signal from a full Wheatstone bridge torque transducer that locks the shaft in place during locked rotor operation.

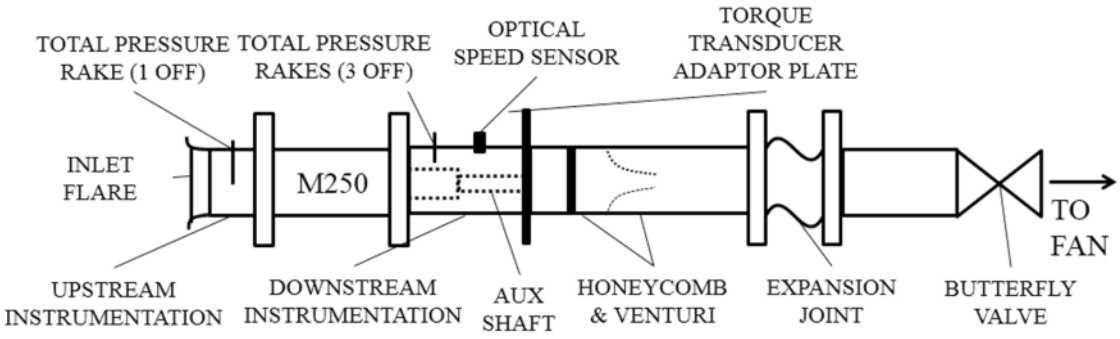

Fig. 2 – Schematic of the M250 sub-idle rig.

The rig arrangement is shown in Figure 2. The torque transducer is placed on an adaptor plate while a groove in a compressor shaft extension allows the coupling of the transducer as shown in Figure 3. The shaft speed is measured via an optical speed sensor that reads off a reflective tape placed on the shaft extension.

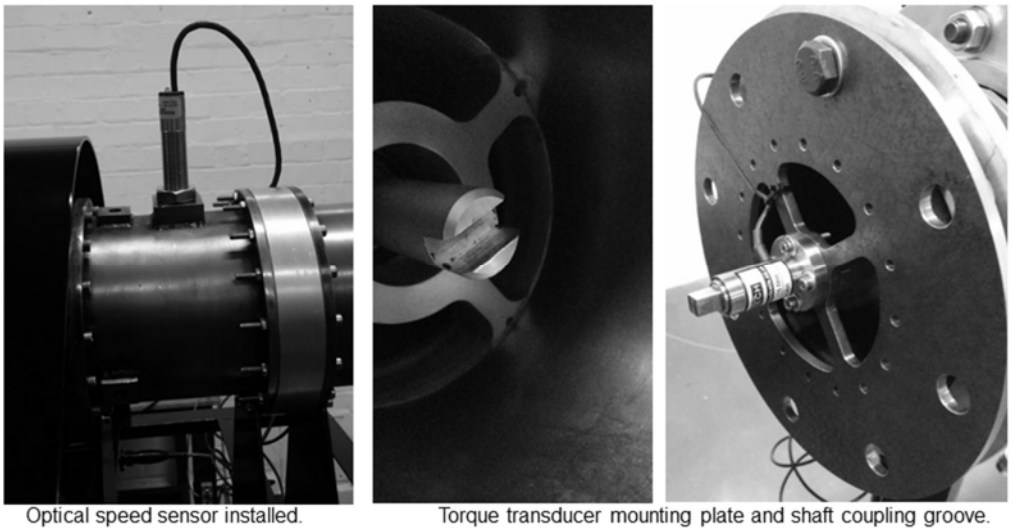

Fig. 3- Optical speed sensor (left), shaft extension (center), and torque transducer (right).

2.2. RANS CFD

The compressor geometry has been supplied by the sponsoring company as a table of design flow angles per blade profile section. From this data and knowledge of the blade thickness distribution, the blade geometry is generated. Tip gaps are estimated from design drawings and modelled but tip gap uncertainty is not assessed. A model is run to design point conditions to ensure the geometry is a true representation of the original.

ANSYS CFX is used in this investigation. This commercial flow solver employs pseudo-transient time stepping and an algebraic multigrid method to advance the solution to a converged steady state. In this investigation, high-resolution advection is used. This results in a total variation diminishing (TVD) scheme seeking to employ second-order upwinding where possible, with a blending factor to a first order upwind scheme as required to enforce a boundedness criterion required by the TVD condition (Ansys, 2016). All simulations are run on Cranfield University's Delta High-Performance Computing cluster with bash scripting to generate CFX Command Language input files to generate automatically the characteristics. The scripting approach is similar to that described in (Pawsey et al., 2018). Convergence for all simulations is based on mass and momentum imbalances reaching values below 0.1% and steady pressure ratio and torque parameters (< 1% variation for torque and negligible variation in pressure ratio). The Shear Stress Transport (SST) model (Menter, 1994) is used to close the RANS equations.

2.2.1. Meshing

The ANSYS Turbogrid meshing software is used for mesh generation, allowing good quality hexahedral meshes to be created rapidly. A grid convergence study on the full compressor geometry for all points under investigation would be prohibitive with regards to computational resources. In order to assess the mesh sensitivity, a single passage model of the first two stages is used. Boundary conditions for this study are zero RPM (locked rotor), total pressure inlet at 1 atm and a mass flow outlet condition set to 10 % of design point mass flow. These conditions correspond to a challenging sub-idle operating point with high negative incidences in excess of -40 degrees and large areas of pressure side separation. Starting from a size of 5E4 elements per passage, the mesh size is uniformly refined with a refinement ratio of ~1.5 to obtain 3 different sizes. In order to ensure a proportional refinement insensitive to y-plus, the CFX automatic wall function treatment has been employed (Ansys, 2016). The effect of y-plus and wall resolution on the overall solution is further investigated independently on the full compressor geometry. Overall pressure ratio and torque are the main parameters of interest. The finest mesh is selected which consists of approximately 5E5 elements per blade passage and a normalized cell size of 0.47 (with coarsest mesh having a normalized cell size of 1). The mesh is determined to lay in the asymptotic region of grid convergence for the selected parameters. Spatial discretization errors are estimated based on the Grid Convergence Index with a safety factor of 1.25 and are deemed to be 0.02 % for the pressure ratio and -4.4 % for torque (Roache, 1994). The order of convergence of the method has been assumed to be unity in the grid study to ensure conservative estimates. This is due to the high-resolution treatment employed, which as discussed, does not guarantee second-order upwinding. The effective order of convergence on the torque parameter was calculated as 1.7.

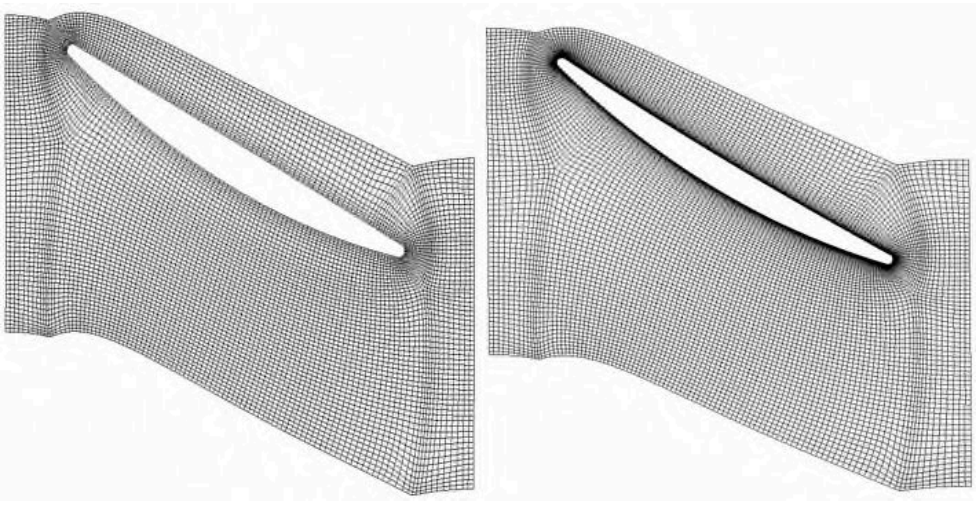

Fig. 4- Wall function mesh (left) and wall resolved mesh (right). Geometry altered due to confidentiality.

The high negative incidence occurring at sub-idle conditions causes the flow to separate abruptly near the leading edge (Illana et al., 2013). Since turbulent recirculation dominates the flow, it is expected that the viscosity-affected sub-layer will not play a determining role in overall compressor performance. However, wall-function approaches may also not be particularly suited to these kinds of flows (Wilcox, 1993). In order to assess the impact of the wall modelling strategy, two mesh sizes are generated for results comparison: a wall-function mesh with y+ ~ 30 and a low-Reynolds mesh with y+ <2. An example of these meshes is given for one of the compressor blades in Figure 4. In order to obtain good quality meshes with y+ < 2, the average node count per passage must be increased to ~1E6 when using the 5E5 mesh as a baseline. Due to its proven robustness and automatic wall function approach, the CFX shear-stress transport (SST) turbulence model is used. This model automatically applies wall functions when the wall y+ is too large to allow integration to the wall, allowing us to ensure physical solution even in those locations where the wall may be locally under-resolved (Ansys, 2016).

2.2.2. Interface models

One of the most critical aspects in turbomachinery CFD is the handling of the interface between different blade-row domains. While mixing planes are generally used for steady-state solutions, such an approach is deemed inappropriate in the case of a locked rotor simulation. The CFX mixing plane domain pitch-change model applies a circumferential band average on the flow field at the interface between blade-row domains. Such an approach relies on the assumption that the relative motion between the rotor and stator is sufficient to mix out the blade wakes instantaneously. An alternative to the mixing plane model is the frozen rotor approach. The frozen rotor approach does not involve mixing and applies a change of frame to account for moving rotor blades such that the relative position of blading remains constant. In addition, the frozen rotor model scales the fluxes to account for un-equal pitches. This model can be applied to cases where the mixing plane approach is not justified, such as when circumferential variation in the flow is large with respect to the pitch and when mixing due to the rotational speed can be neglected. However, the frozen rotor approach introduces an additional variable, as the relative tangential position now becomes an additional parameter that could influence results. An approach to mitigate this may be to model different relative positions and phase-average the result. For high speeds, this may yield comparable results to mixing plane formulations that require lower computational resources. For low speed cases with large separated wakes (locked rotor being an extreme such case) frozen rotor approaches may be more desirable to capture the effect of the wake on downstream stages. The choice between the two methods must be considered as it pertains to the specific case being modelled and computational resources available (Ansys, 2016). Ultimately, turbomachinery is an inherently unsteady process, so the choice of a steady-state interface model will always involve an assumption.

While the mixing plane approach can be applied to any configuration with different blade pitch between stages, methods not employing mixing planes would require multiple passages to be modelled in order to match the domain pitch at the interface (Erdos & Alzner, 1978). A traditional approach to matching un-equal pitch gaps is to scale the geometry such that a revised blade count is used for each stage, ensuring domain pitches match at interfaces. A disadvantage of this approach is that passage geometry is altered, so parameters like blade solidity no longer represent the original geometry. As such, compressor models with unequal pitches will need several passages to be modelled, which could result in large domains. In the absence of rotational speed, the frozen rotor model simply acts as flow scaling model in the case of un-equal pitches. It is used here for the locked rotor case in order to allow a multi-stage compressor with un-equal pitches to be modelled without the need to model the entire annulus or scale the compressor geometry itself. While the frozen rotor approach is used to allow flux scaling at interfaces, the inaccuracies introduced by the scaling need to be mitigated by ensuring a pitch ratio near one throughout the compressor. For the M250 compressor, a 50 deg sector annulus has been employed in frozen-rotor implementations to minimize flux scaling between unequal pitches and allow different relative tangential positions to be considered. Preliminary comparative studies showed sector models comprising 100 deg did not result in noticeable differences respect to the 50 deg model. The wall-resolved mesh used in this study amounted to a

total of 36E6 elements for a 50 deg sector simulation. The wall function mesh amounts to 20E6 elements for the same configuration, while employing mixing planes and a single passage model reduces the mesh requirement to 7E6 elements, a size amenable for solution on a desktop workstation. The difference in mesh sizes from the choice of interface model highlights the trade-offs that need to be kept in mind when selecting an interface. This will be highly dependent on the compressor blade counts, with the use of prime numbers and high blade counts in modern compressors making pitch matching more difficult. A model showing a sector simulation of the M250 compressor is shown in Figure 5, highlighting the large models that might be generated in trying to obtain pitch ratios near unity with a frozen rotor simulation. Figure 5 also shows the boundary conditions applied to the models. The geometry shown has been altered due to confidentiality reasons and does not represent the true compressor.

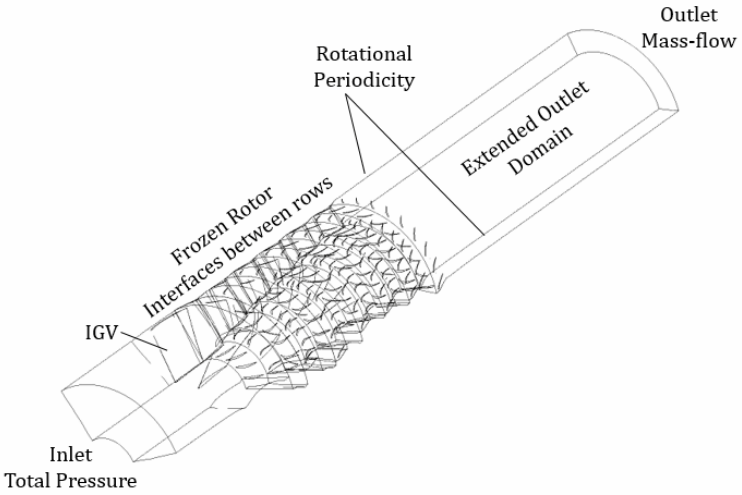

Fig. 5- Sector annulus model and boundary conditions.

Unlike the locked rotor case, the mixing plane approach could arguably be applicable to the windmilling case due to the rotational speed that allows wake mixing, incurring an entropy generation. To ascertain this assumption, models were created for both the frozen rotor and mixing plane approach to be compared against experiment for the torque-free windmill cases. Results from the two models are included in the results section.

In order to find the torque-free windmilling point, a CEL (CFX Expression Language) expression was used to alter the mass flow boundary condition until a net zero torque was obtained on the compressor blade surfaces for a given rotational speed. Eq. 3 shows a simplified version of the expression used. The "if" statements ensure the boundary condition is only updated after a specific number of iterations determined by the k parameter and after the standard deviation on the torque value over the past k iterations has dropped below a tolerance value. These statements multiply the mass-flow adder by 1 only if the condition evaluates to true. This ensures the solution has had time to stabilize before the boundary condition is updated once again. Additional logic not shown in Eq. 3 ensures that the absolute change in the mass-flow value is limited to 10% of the current mass-flow, in order to avoid excessively aggressive boundary condition changes which may cause numerical instabilities. A further relaxation parameter, ζ, can also be used to ensure flow boundary condition is not varied too aggressively. A more involved method, perhaps employing a Newton-Raphson scheme could also be employed, but this would require knowledge of the parameters at previous time-step, which would require a more complex implementation. This simple approach using CEL expressions has proven to be robust.

$$\dot{m}_{\text{new}} = \dot{m}_{old} + \zeta \times \tau \times if(mod(itern, k) == 0,1,0) \times if(\sigma_\tau < tol, 0,1,0) \quad (3)$$

An interrupt condition was used to stop the solution once the root mean square of the torque over a given number of iterations had reached a specified tolerance.

2.2.3. Steady vs. unsteady models

The applicability of using a steady state analysis under such separated flow conditions is considered. It is expected that for time-averaged performance parameters such as pressure ratio and torque, a steady state assumption will be sufficient. However, oscillatory convergence in the torque parameter as solutions are marched towards a steady-state solution points to the need for investigating time-accurate solutions (Spalart & Venkatakrishnan, 2016). The effect of oscillatory convergence can be accounted for alongside the GCI values to estimate the numerical uncertainty in the model. Based on this approach, and using a 95% confidence interval, numerical uncertainty for pressure ratio is calculated as being always below 0.3%, including convergence and GCI considerations. For torque however, the highest torque uncertainty obtained is 9.6% for the lowest mass flow locked rotor case using the M250 model. For locked rotor cases other than the lowest mass flow, torque uncertainty remains always below 7% including both GCI and oscillatory convergence considerations. As the unsteadiness under high negative incidence is due to vortex shedding rather than an external forcing function, the lack of a spectral gap requires some form of scale resolving simulation (Tucker, 2011). Generating characteristics with a time-accurate, scale-resolving, multi-stage compressor model is a prohibitive proposition, so a single-stage model is instead created to assess the limitation of steady RANS at the conditions studied. A study of scale-resolving simulation for sub-idle conditions is given in (Iglesias, 2018) and is out of scope of this work. The unsteady modelling is only assessed here as it pertains to the performance parameters under consideration.

A single-stage model is developed to compare the results of steady RANS against URANS and two scale resolving models: Scale Adaptive Simulation (SAS) and Stress Blended Eddy Simulation (SBES) (Menter, 2015). The SAS can be formally described as an improved URANS model, since the SST turbulence equations are solved, albeit with a modification on the eddy frequency (ω) equation. This modification pertains to the addition of a term to adjust the length scale based on the local von Karman length scale, thereby adjusting the model to the turbulent structures already resolved in the flow. This lack of adjustment is the common ailment of standard URANS implementations (Menter, 2015). The Stress Blended Eddy Simulation is a hybrid RANS-LES implementation similar to other approaches like the Detached Eddy Simulation (DES) model family. The main difference between SBES and the DES approaches is the use of a shielding function to blend the stress tensors obtained separately from RANS and the selected LES sub-grid scale models. This is in contrast to DES-type approaches where the LES model is still a form of the underlying RANS equations (Menter, 2015).

The geometry consists of a mid-stage rotor and stator of a modern core compressor. A transient rotor-stator interface is used between the rotor and stator domains, with a profile transformation model applied to handle un-equal pitches. This profile transformation interface is similar in concept to the frozen rotor approach regarding flux scaling, but the unsteady convection of wakes between moving frames is considered. The pitch ratio for the model used is 0.93 with a sector angle of approximately 10 degrees. The model has been extended by 3 blade chords upstream and 10 blade chords downstream in accordance with best practice guidelines (Ansys, 2016). A schematic of the model used is shown in Figure 6.

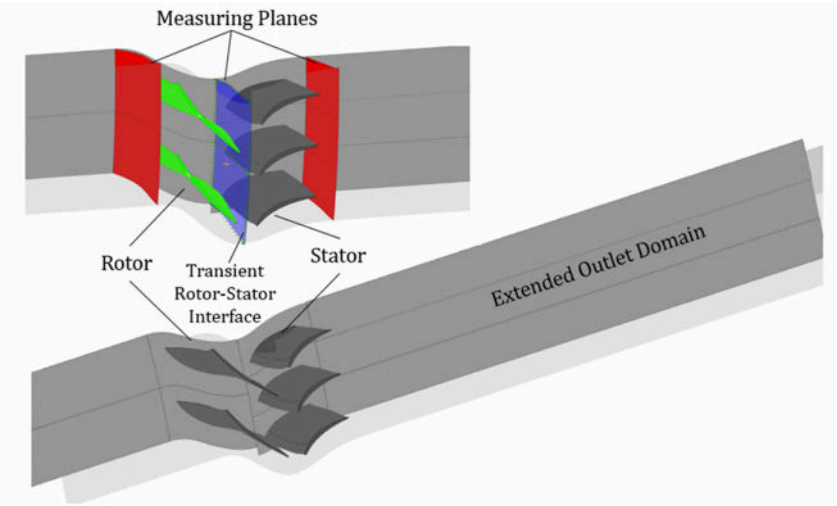

Fig. 6- Single-stage model for unsteady studies.

In terms of meshing, best practices for the SAS model call for grid size comparable to the expected turbulent length scales. A wall-resolved RANS mesh covers this requirement with grid sizes ~ 1% of the blade chord in scale resolving zones. For the SBES model, a mesh with grid sizes ~ 0.7% of the blade chord in the scale resolving zone has been selected (Iglesias, 2018). Meshes consist of approximately 1.3E6 and 3.5E6 elements per passage for the RANS and SBES cases respectively. A representative Reynolds number for the flows investigated is 1E5 based on blade chord. The adequacy of a scale-resolving mesh can be assessed from an analysis of the amount of turbulence resolved vs. the amount that gets modelled by the underlying RANS closure. In the ANSYS CFX implementation of SBES, a shielding function controls the blending between the RANS and LES Reynolds stresses. An explicit switch is made to an algebraic LES model in regions where the SBES shielding function is null, whereas the underlying RANS model (SST in this case) is used in regions where the shielding function is unity (Ansys, 2016). Figure 7 shows how only the near-wall region is captured by the model, while the rest is covered by an algebraic LES formulation. The mesh resolution used has resulted in 3% of the turbulence kinetic energy being modeled at the stator outlet plane.

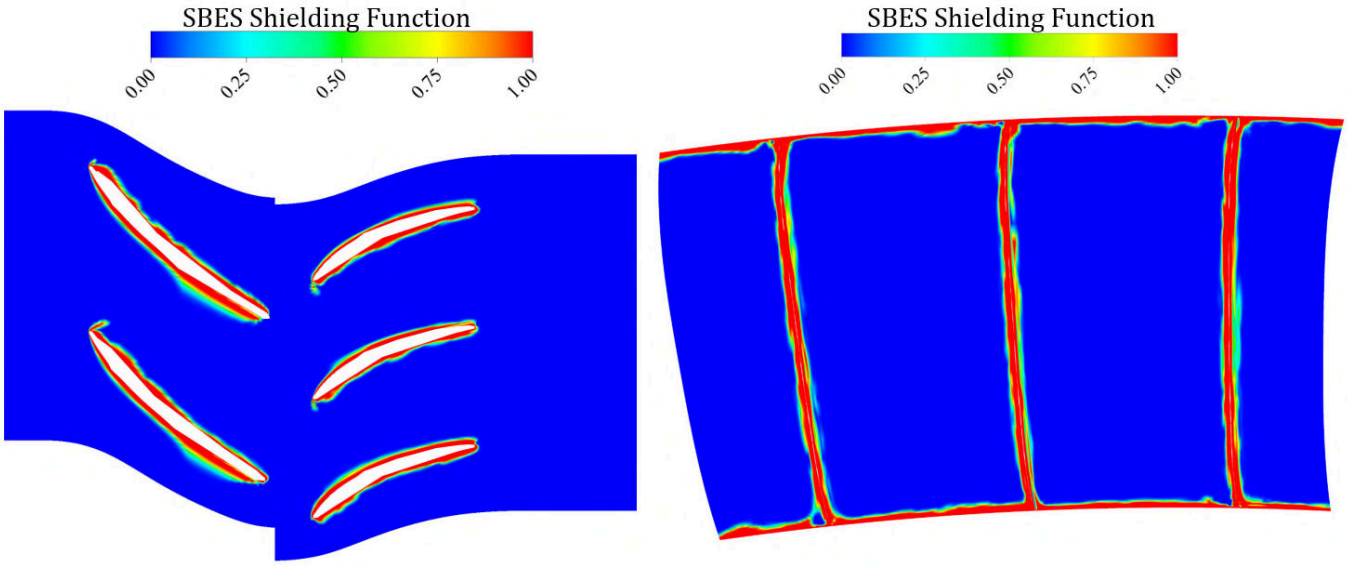

Fig. 7- SBES shielding function at 50% span cut (left) and at a constant axial location immediately downstream of stator trailing edge. (Airfoil geometry altered due to confidentiality).

3. .Results & Discussion

3.1. Unsteady simulation

Results for the locked rotor single stage are shown in Figure 8 comparing time average pressure ratio contours between RANS and the different unsteady models. While all models capture mostly the same flow features, the scale resolving models show a more diffuse pattern. This can be reasoned from the presence of unsteady turbulent structures not captured in the RANS formulation. A frozen rotor interface is used for the steady RANS case, while a transient rotor-stator interface is used for all unsteady cases.

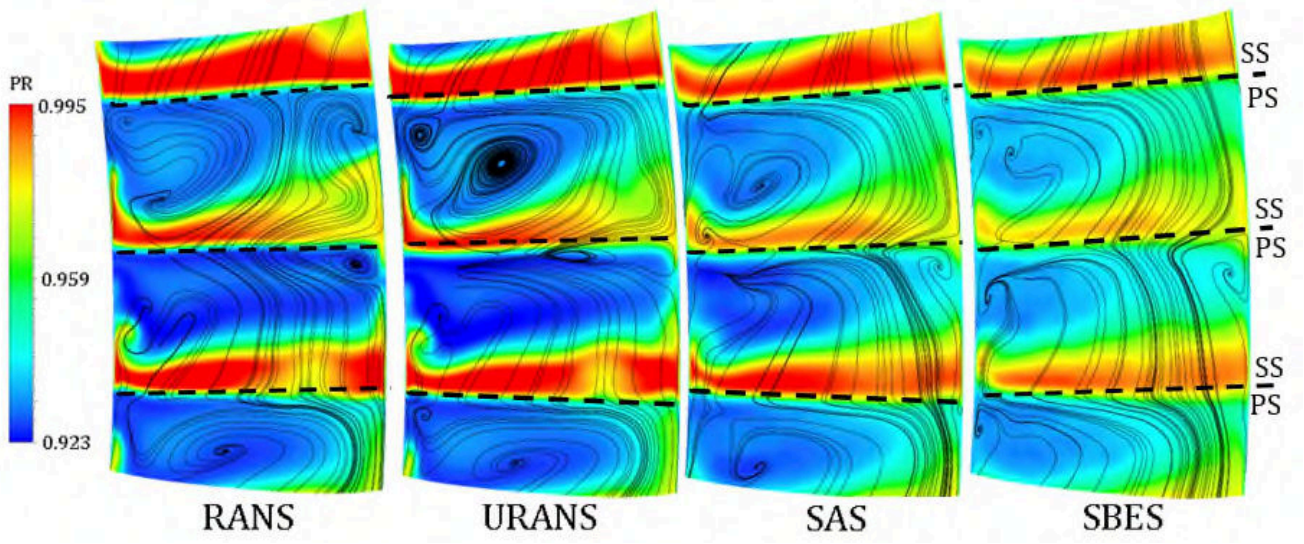

Fig. 8- Comparison of RANS vs. time-averaged unsteady models for a single stage locked rotor at 16% of design corrected mass flow (Re ~ 8E4). The plane shown in all cases corresponds to stage exit at the stator trailing edge.

Figure 9 compares the time-averaged SBES Mach number against the RANS solution on a cascade plane at 50% span. RANS is seen to predict a separation bubble that stretches further downstream than the SBES solution. Figure 10 shows the spanwise vorticity on the same cascade plane. The spanwise vorticity can be used to investigate the extent of the pressure and suction side boundary layers as done in (Leggett et al., 2016). This figure shows that the pressure side dominates boundary layer detaches and dominates the channel. More importantly, Figure 10 shows the differences between the RANS and SBES simulations at these conditions, with the longer separated boundary layers consistent with the observations in Figure 9. The differences between the predicted vorticity fields have been highlighted on the RANS plot. RANS predicts longer shear layers and does not capture the intermittent boundary layer reattachment that causes the higher vorticity seen on the pressure side trailing edge in the SBES case. From a machine performance perspective, this may cause differences in the predicted torque on the blading.

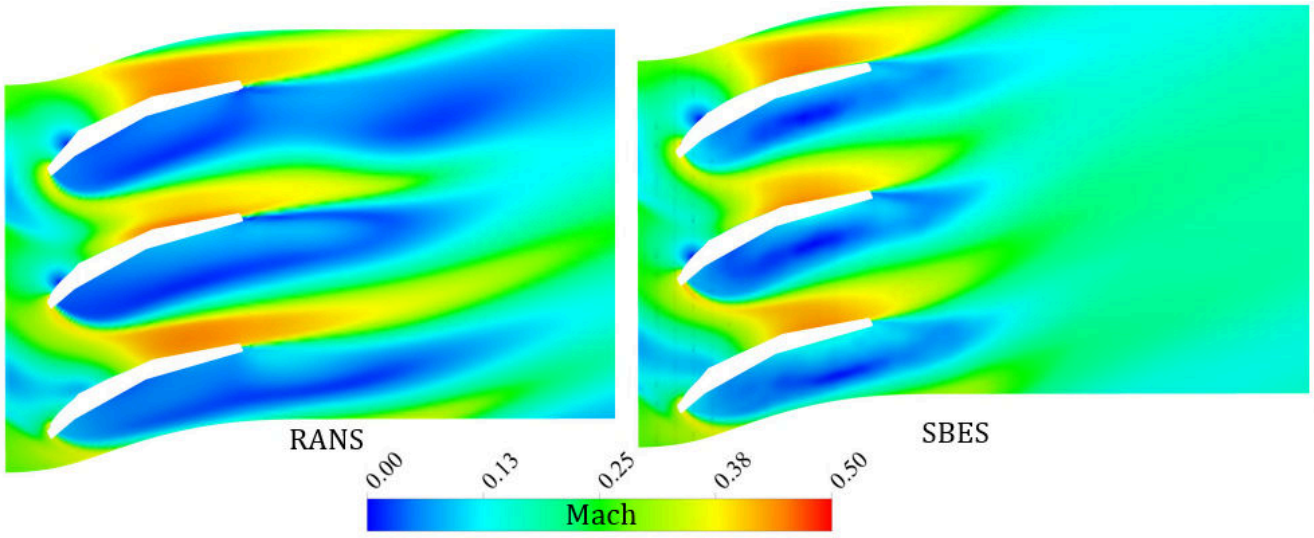

Fig. 9- Comparison of RANS vs. time-averaged SBES Mach number for a single stage locked rotor at 20% of design corrected mass flow (Re ~ 1E5). (Airfoil geometry altered due to confidentiality).

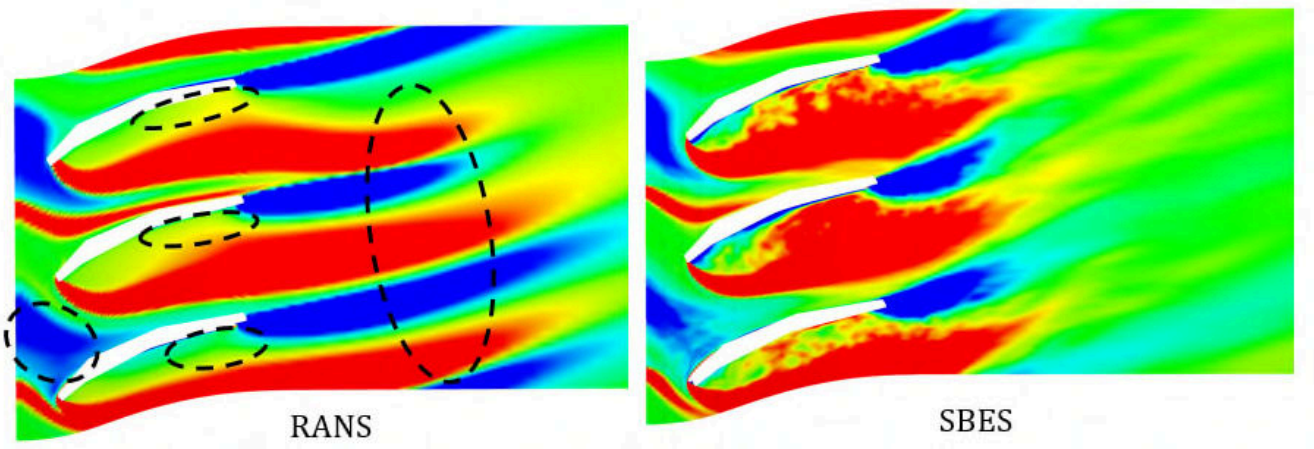

Fig. 10- Comparison of RANS vs. time-averaged SBES spanwise vorticity for a single stage locked rotor at 20% of design corrected mass flow (Re ~ 1E5) Vorticity contours span -1E4 Hz to 1E4 Hz. (Airfoil geometry altered due to confidentiality).

Figure 11 shows the differences in the pressure ratio and torque characteristics calculated. The average percent difference between the torque and pressure ratio values computed by each of the methods and those predicted from RANS are presented in Table 1. The differences in pressure ratio are negligible, while differences in torque are not. Judging by the torque parameter, the SAS and SBES models appear comparable for obtaining time-averaged performance parameters. The difference between the RANS and SBES solution for torque is ~5%. Based on these results, it is considered that a steady-state approach can be acceptable to obtain adequate performance representation from a bulk parameter perspective, but that judgement must be exercised in the values of torque obtained. Moreover, it is important to note that while the RANS simulations may capture the broad performance trends investigated here, detailed flow mechanisms would not necessarily be captured equivalently by RANS and hybrid methods, as can be evidence from the brief discussion on the size of the separated regions given above. A recent investigation into this phenomenon as it regards loss prediction can be found in (Leggett et al., 2018).

Table 1 – Locked rotor CFD transient models. Difference from RANS solution.

Model	URANS	SAS	SBES
Pressure Ratio	0.0204 %	0.0313 %	0.0707%

Torque	0.680 %	4.0236 %	4.8747 %

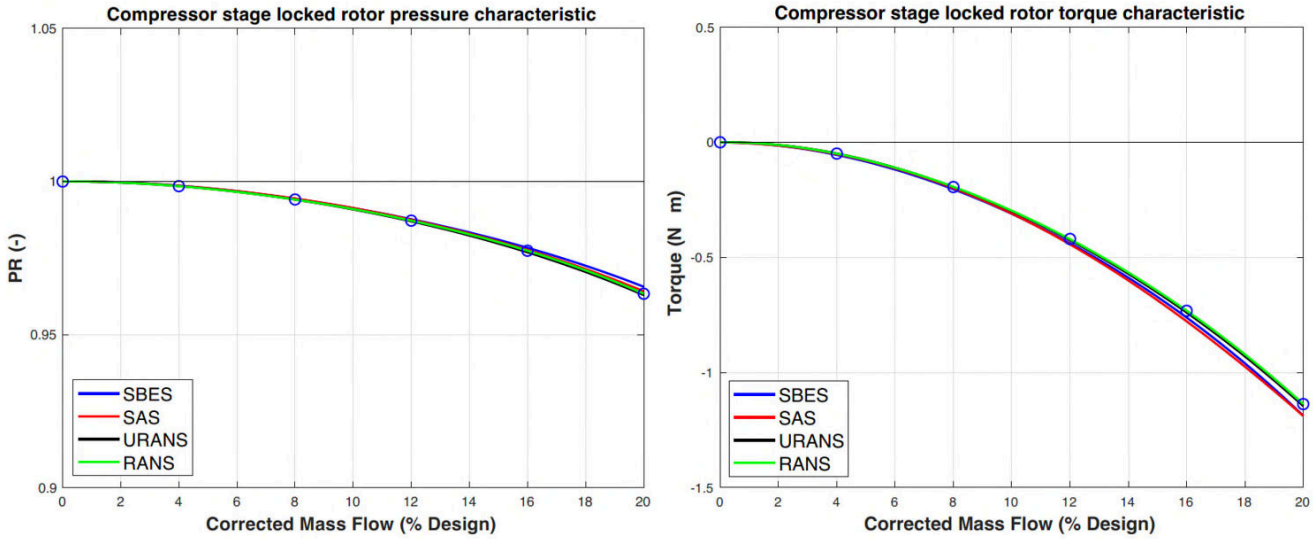

Fig. 11- Comparison of RANS characteristics vs. different transient models for a single stage locked rotor.

3.2. RANS Characteristics vs. experiment

Pressure ratio characteristics have been experimentally obtained for both the locked rotor and windmilling cases. In addition, a torque characteristic is obtained for the locked rotor case while a shaft speed vs. corrected mass flow line is obtained for the windmilling case. Data is gathered at each mass-flow point using 1 minute sample times and a 5 Hz sampling rate, resulting in 300 samples per operating point. Error bars for experimental points in Figures 12, 14 and 15 report combined standard uncertainty, including propagated instrumentation uncertainty and standard error of the mean at each point. Numerical results include uncertainty bars that include GCI and iterative convergence estimated errors. No such error bars are included for shaft speeds as that is a model input. A series of locked rotor and windmilling mass-flow points have been selected using the rig's buttefly valve. Due to the losses incurred throughout the test apparatus, the mass flow points reachable are limited by the extraction fan's static pressure rating. In this manner, only a partial characterization of the locked-rotor and windmill characteristics can be obtained. This is however deemed sufficient for an assessment of the numerical models to be carried out.

3.2.1. Locked rotor

The locked rotor experimental and numerical results are compared in Figure 12. Three different numerical models are compared as described in Table 2. Two principal aspects are investigated here: the use of a multiple-passage vs. a single passage domain and the use of a wall-resolved mesh vs. a wall-function mesh. All locked rotor models employ a frozen rotor domain pitch-change model.

Table 2– Locked rotor CFD models

Domain Model	**50 deg sector Frozen Rotor**	**50 deg sector Frozen Rotor**	**Single Passage Frozen Rotor**
Wall y+	<2	30	30
Node count per passage	~1.1E6	~0.5E6	~0.5E6

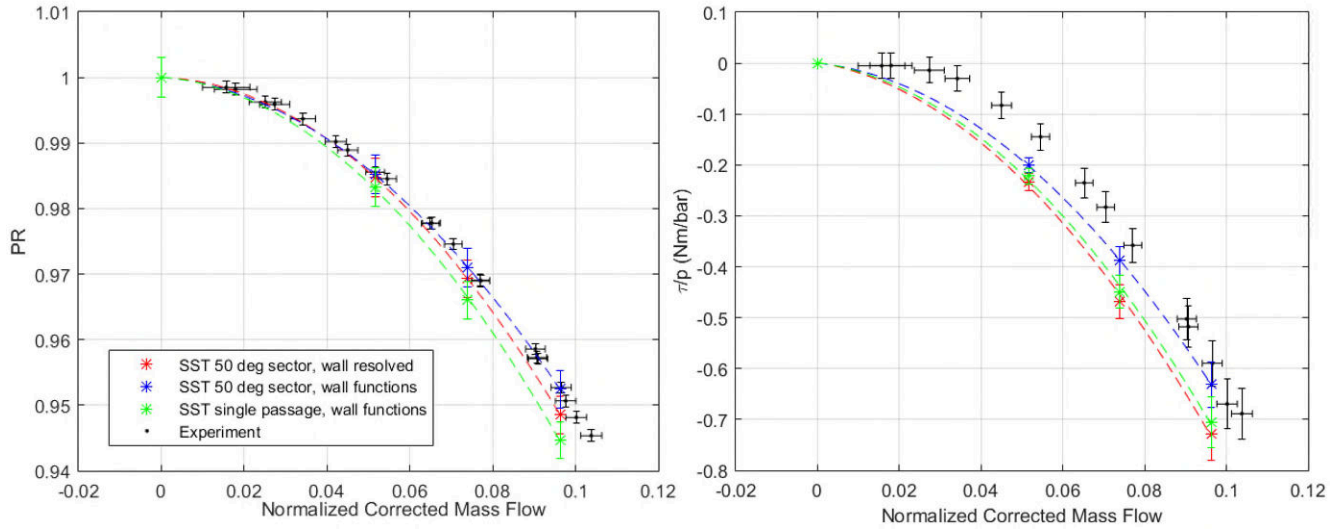

Fig. 12- Comparison of RANS locked rotor pressure ratio (left) and torque (right) characteristic vs. experiment.

As expected from preliminary single-stage unsteady results, pressure ratio is better matched than torque. Of the models tested, the multiple passage wall-function approach yields the best results, especially for the pressure ratio characteristic. The lowest mass flow portion of the locked rotor characteristic cannot be accurately obtained numerically, but the condition of zero torque and no losses at no mass flow yields the extremum of the sub-idle map. The locked rotor pressure characteristic has a quadratic shape, as the compressor acts like a cascade and losses are directly proportional to the inlet dynamic pressure. This points to the notion that a single locked rotor simulation, along with a zero slope condition at the origin, could be used to build a notional locked rotor line from which to build a sub-idle map. A similar procedure could be used to approximate a torque characteristic. While there may exist some discrepancies in the torque matching, the low absolute difference (~ 0.1 N-m) may be considered acceptable from a performance map standpoint, especially when other assumptions inherent in steady-state performance modelling are considered.

A locked-rotor flow-field obtained from numerical simulations is shown in Fig. 13. This highlights the negative incidence flow and pressure side separation expected at these conditions (Illana, 2013). The wake structure justifies the use of a frozen rotor approach, as the wakes do not instantaneously mix and span into downstream stages. The slight flow-field distortion seen in between blade domains in Fig. 13 is due to the frozen rotor flux scaling applied to domain pitches not being exactly equal. As opposed to high-speed compressors, low-speed compressors begin choking from the rear, due to the lack of compression and geometric contraction of the flow-path, and the formation of a throat on the suction side of the blade is seen. Approximating the blading as flat plates, incidence values at the last stator are ~ -60 degrees. For the lowest mass-flow point simulated on the locked rotor line, Reynolds numbers based on average chord vary from 5E3 at IGV inlet to 2E4 at the last stator, with 1E4 to 5E4 being representative of the average range throughout the locked rotor line.

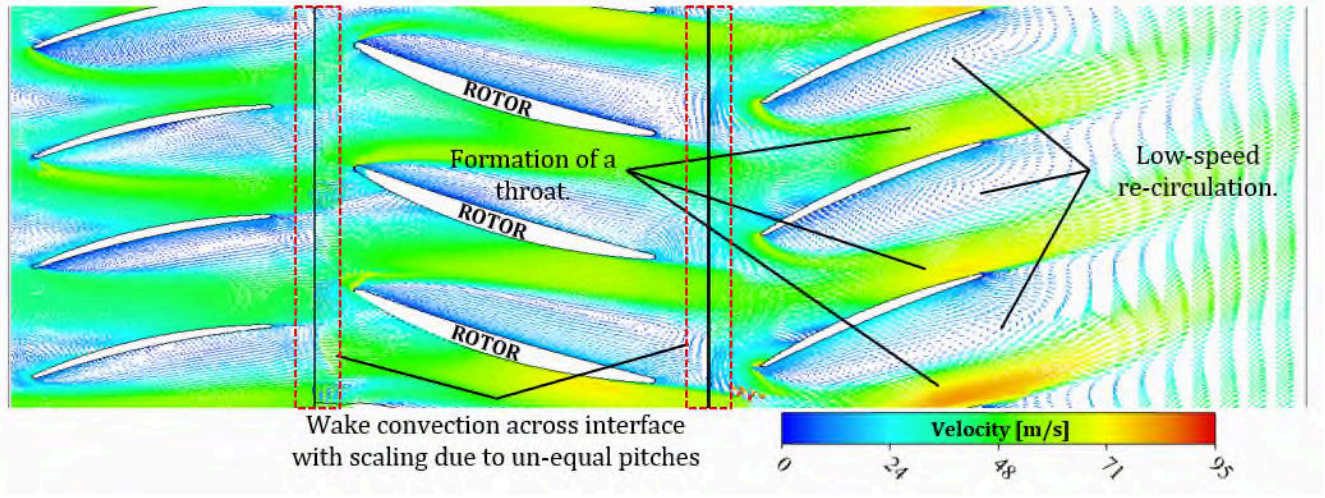

Fig. 13- Flow-field in rear stages for locked rotor operation at 7% design point corrected mass flow Geometry altered due to confidentiality.

3.2.2. Torque-free windmill

The windmill line is obtained using the procedure previously described, where the solver varies the outlet mass flow boundary condition until zero torque is measured on the compressor blading. Two models are tested here: the frozen rotor 50 deg sector model with a wall resolved mesh and a mixing plane model with a wall-function mesh. This choice is made to test the two extremes regarding computational requirements. These are summarized in Table 3. Comparison between experimental and numerical results are shown in Figure 14. Starting from a converged solution of a case at the same target speed, the single passage model was able to converge to a torque-free windmill condition in under 300 iterations during an overnight simulation on a standard desktop using 6 cores.

Table 3 – Torque-free windmill CFD models

Domain Model	**50 deg sector Frozen Rotor**	**Single Passage Mixing Plane**
Wall y+	<2	30
Node count per passage	~1.1E6	~0.5E6

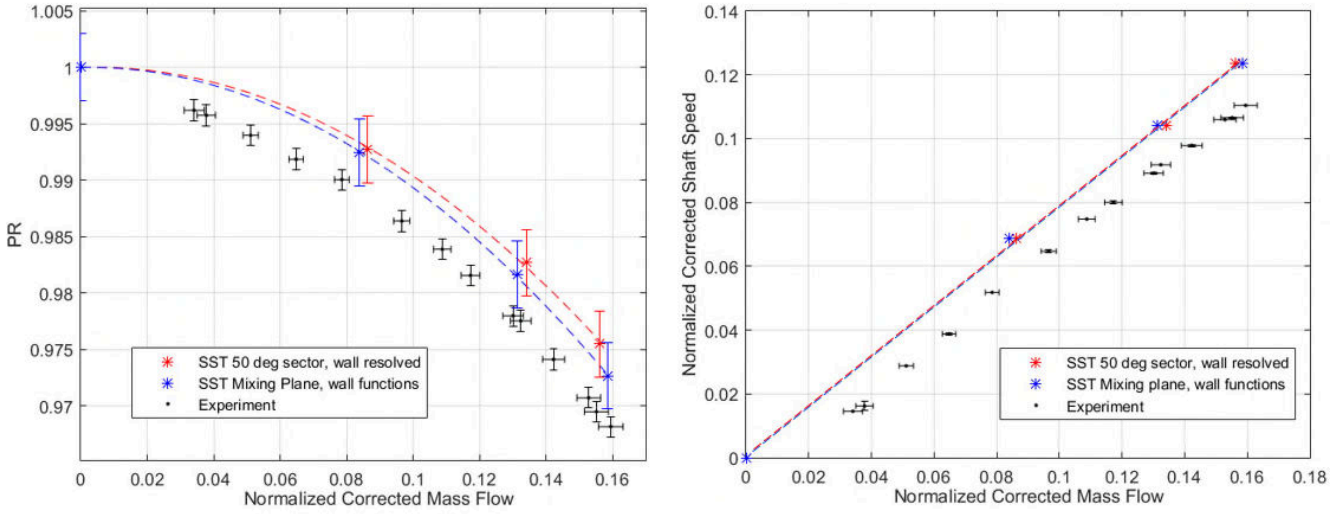

Fig. 14- Windmill pressure ratio characteristic (left) and windmill line (right) from CFD and experiment.

The windmill numerical models predict faster windmilling speeds than those measured experimentally. This discrepancy on the windmill results can be explained from the torque-free condition imposed on the CFD model. While a zero torque condition is imposed on the numerical model, the experimental windmill line is not truly torque free. Frictional losses exist on the rig's shaft along with a static frictional torque that must be overcome before a steady-state windmill speed is reached. This discrepancy on the windmill speed could also be partly to blame for the higher predicted pressure ratios, as the experimental compressor is actually operating marginally within the turbine region as defined in Figure 1. In order to assess the ability to match the experimental windmilling point numerically, another set of simulations with the mixing plane model are performed taking into account the existence of resistive torques. The mixing plane model only is used due to its lower computational expense (as single passage is modelled instead of several) and its comparable performance to the frozen rotor multi-passage model.

Using an experimental windmill flow-speed pair as boundary conditions to obtain an estimate of the resistive torque acting on the rig, a negative shaft torque of -0.15 N-m is found to be an appropriate estimate. This negative torque is due to frictional resistance in the rig and can be used within Eq. 3 instead of the zero-torque condition in order to match the rig's shaft friction. Figure 15 shows how the pressure characteristic matching is improved as result of matching rig conditions, with limited effect on the predicted windmill signature (slope of windmill line). The windmill line is now seen to shift to the right as higher mass flow is required at the same rotational speeds, matching the experimental data. A true frictional model would take into account the shaft speed; however, this quick verification shows that a resistance model along with the methodology described can be used to obtain accurate windmill predictions under realistic conditions where friction, or other torque loads such as driven pumps, must be taken into account.

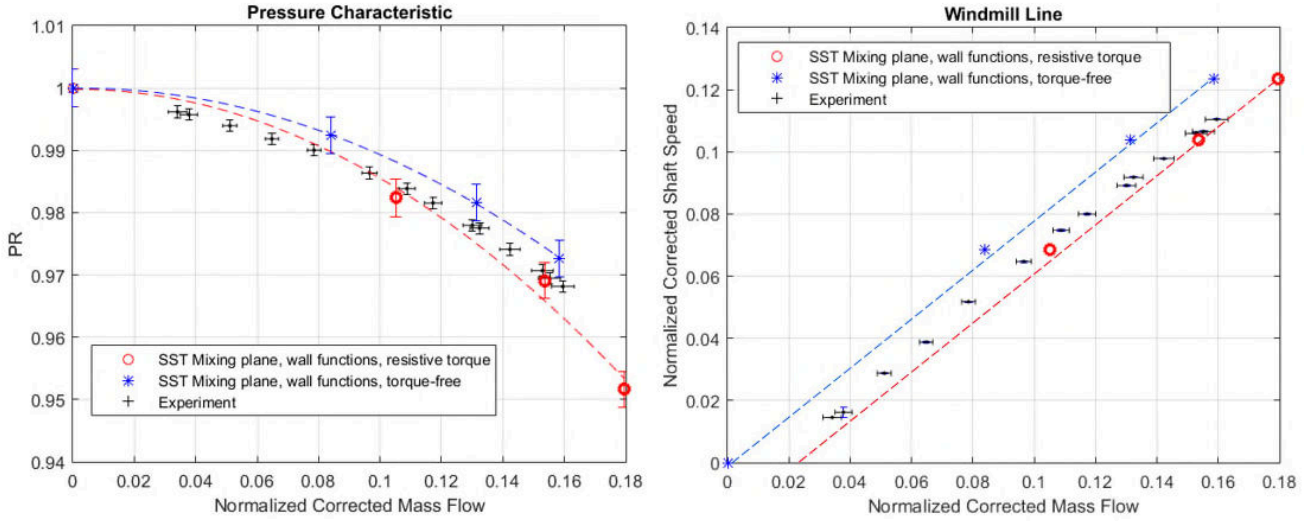

Fig. 15- Windmill pressure ratio characteristic (left) and windmill line (right) from CFD and experiment with and without resistive torques.

The accuracy of the CFD models can be assessed based on the windmill speed to mass flow slope. This slope is analogous to the windmill flow coefficient, and can be very useful in characterizing a compressor's sub-idle performance. This has previously been referred to as the compressor's "windmill signature" (Ferrer-Vidal et. al, 2018). The windmill signatures predicted by each model are compared here against experiment in Table 4. The mixing plane model yields a discrepancy of 1.85 %, justifying its applicability in windmill speed prediction.

Table 4 – Torque-free windmill signatures

	Normalized Windmill Signature	Relative Discrepancy
Rig	0.77	-
Frozen Rotor	0.79	3.25 %
Mixing Plane	0.78	1.85 %

Whereas the frozen rotor pitch-change model is considered the most appropriate to account for unequal pitches in the locked rotor case, no considerable difference is seen between frozen rotor and mixing plane models for the torque-free windmill cases. For the M250 frozen rotor 0.12 N_p torque-free windmill case, Figure 16 shows the velocity flow-field in the rear stages of the compressor, where separation is highest. The flow-field separation is not as dramatic as in the locked rotor case of Figure 13, with the wakes now occupying a smaller pitch fraction. The fact that circumferential variation in the flow-field is relatively small indicates that a mixing plane approach could be an appropriate steady-state approximation (Ansys 2016). The mixing plane approach requires only one passage to be modelled and thus has been used here for the torque-free windmill simulations. Likewise, no benefit has been observed in the use of wall-resolved meshes, so a wall-function approach has been deemed appropriate.

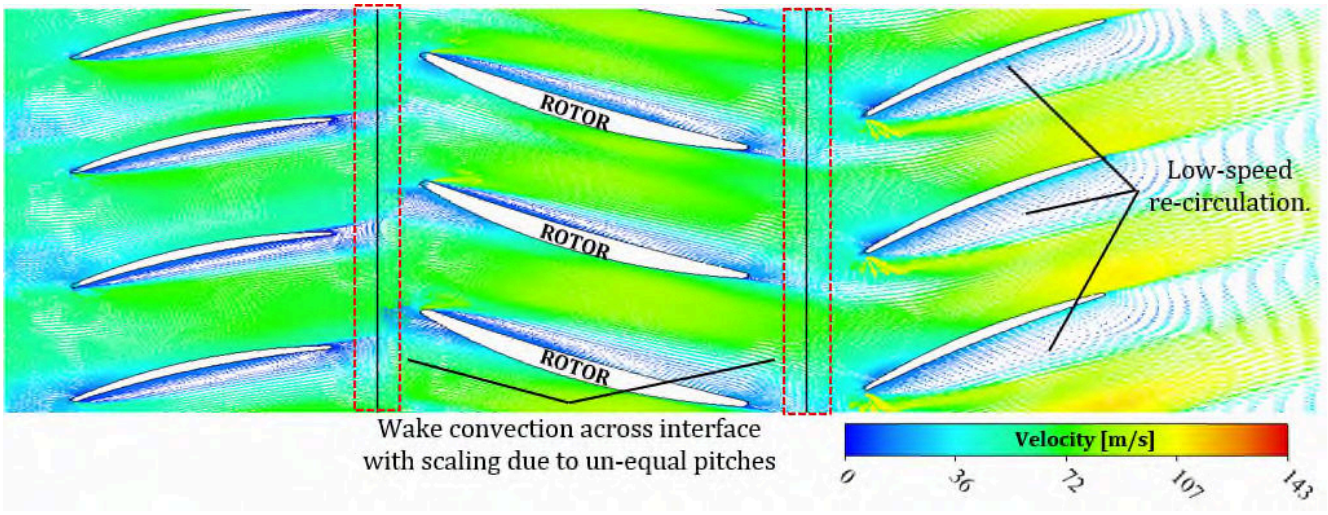

Fig. 16- Torque-free windmill flow-field in rear stages at 11% of design speed. Geometry altered due to confidentiality.

3.3. Multi-stage performance

In addition to the numerical work with the M250 compressor, a modern six stage compressor (M6SC) representative of current architectures is used to study the multi-stage compressor performance at locked rotor and torque-free windmill. The M6SC has a hub-to-tip ratio of ~ 0.7 at the inlet to the first stage, in comparison to hub-to-tip ratio of ~ 0.3 for the M250. Wall function meshes with ~5E5 nodes per blade passage have been used along with an SST turbulence model as previously discussed for the M250.

3.3.1. Locked rotor

At locked rotor, the compressors simply act as rows of cascades incurring pressure losses on the flow and imparting a torque on the shaft. The axial distribution of pressure loss and torque for the M250 and M6SC compressors in terms of normalized pressure loss and normalized corrected torque are shown in Figure 17. In these figures, the rotor labels correspond to the exit from each rotor. The definition of the normalized parameters used are shown in Eq.4.

$$\Pi^* = \frac{\Delta P_{tot}}{\Delta P_{tot_{compressor}}}, \qquad \tau_c = \frac{\tau_{\text{corr}}}{\tau_{corr_{R1}}} \tag{4}$$

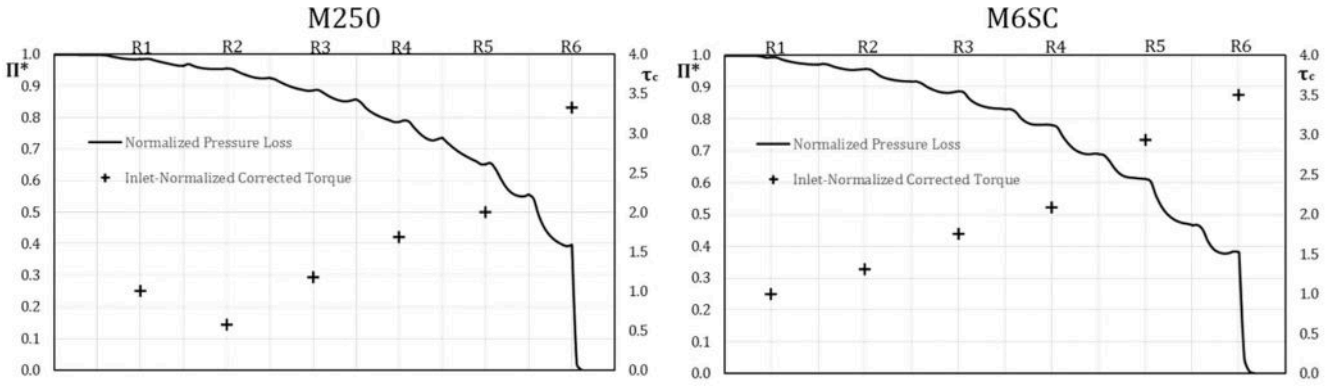

Fig. 17- Locked rotor pressure loss and torque axial distribution for the M250 (left) and M6SC (right) compressors.

As shown in Figure 17, the relative pressure losses through both compressors follow similar trends, with up to 40 % of the overall pressure loss occurring in the last stator. For both compressors, the last rotor produces ~3.25 times the torque of the first rotor, while for the M250 a distinct difference exists in the torque produced by the second rotor, which does not follow the same trend as for the M6SC. This can partly be explained from the compressor geometry, where the second M250 rotor has the same number of blades as the first, and from the presence of an IGV, which increases the negative incidence on the first rotor, increasing its torque with respect to the case of a first rotor without an IGV (as in the M6SC).

3.3.2. Torque-free windmill

During torque-free windmill operation, no net work is imparted on the flow, but this does not preclude individual stages from extracting or doing work on the fluid in a multistage compressor. From the numerical results, axial distributions of loading and pressure rise at the different torque-free windmilling points simulated can be compared. Two parameters normalized by inlet conditions are defined, a stage loading coefficient (ψ) and a total pressure rise coefficient (λ), as follows in Eq. 5.

$$\psi = \frac{\Delta h_{rotor}}{\Delta h_{rotor1}}\,, \qquad \lambda = \frac{\Delta P_{tot}}{\frac{1}{2}(\rho v^2)_{inlet}} \tag{5}$$

Figures 18 and 19 show load coefficient per rotor as well as the axial total pressure rise distribution, with the rotor labels corresponding to the exit from each rotor. The load coefficients and total pressure rise across the compressor are equivalent for each stage at different windmill speeds for both compressors studied. In both cases, the first 4 rotors do work on the flow that is then extracted by the last two stages. Comparison of the load coefficient distribution and axial pressure rise distribution allows the different operating regimes portrayed in Figure 1 to be identified on a stage-by-stage basis. For both compressors, a work addition and pressure rise occurs in the first three stages, consistent with compressor operation. The last two stages show a work extraction and associated pressure loss. In both compressors, work addition in rotor 4 is not accompanied by a total pressure rise, and is representative of the stirrer regime.

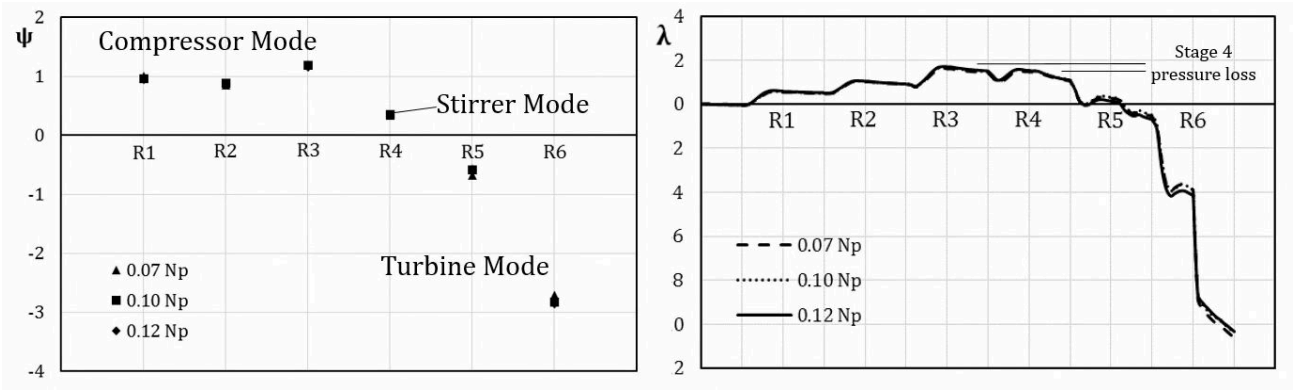

Fig. 18- Windmill load coefficient distribution per rotor (left) and axial total pressure rise distribution (right) for three different torque-free windmill (7%, 10% and 12% design speed) points of the M250 axial compressor.

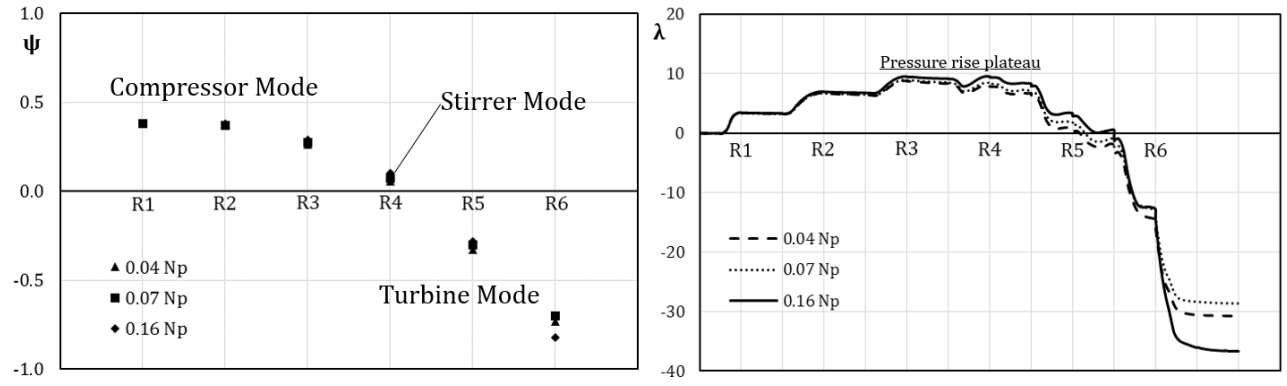

Fig. 19- Windmill load coefficient distribution per rotor (left) and axial total pressure rise distribution (right) for three different torque-free windmill points (4%, 7% and 16% design speed) of the M6SC axial compressor.

The similarity in axial distributions shown in Figures 18 and 19 indicates that different torque-free windmill operational points can potentially be related through scaling. s Such scaling of self-similar flow-fields has previously discussed for windmilling fans (Prasad, 2018). Figure 20 shows flow-field contours for flow (φ) and pressure rise (λ) coefficients for both the M250 and M6SC. Qualitatively similar flow-fields are shown both in terms of flow features and magnitude of the non-dimensional parameters. The same structure of jet and separated regions can be seen. The flow coefficient employed is defined in Eq. 6.

$$\varphi = V_{ax}/U \tag{6}$$

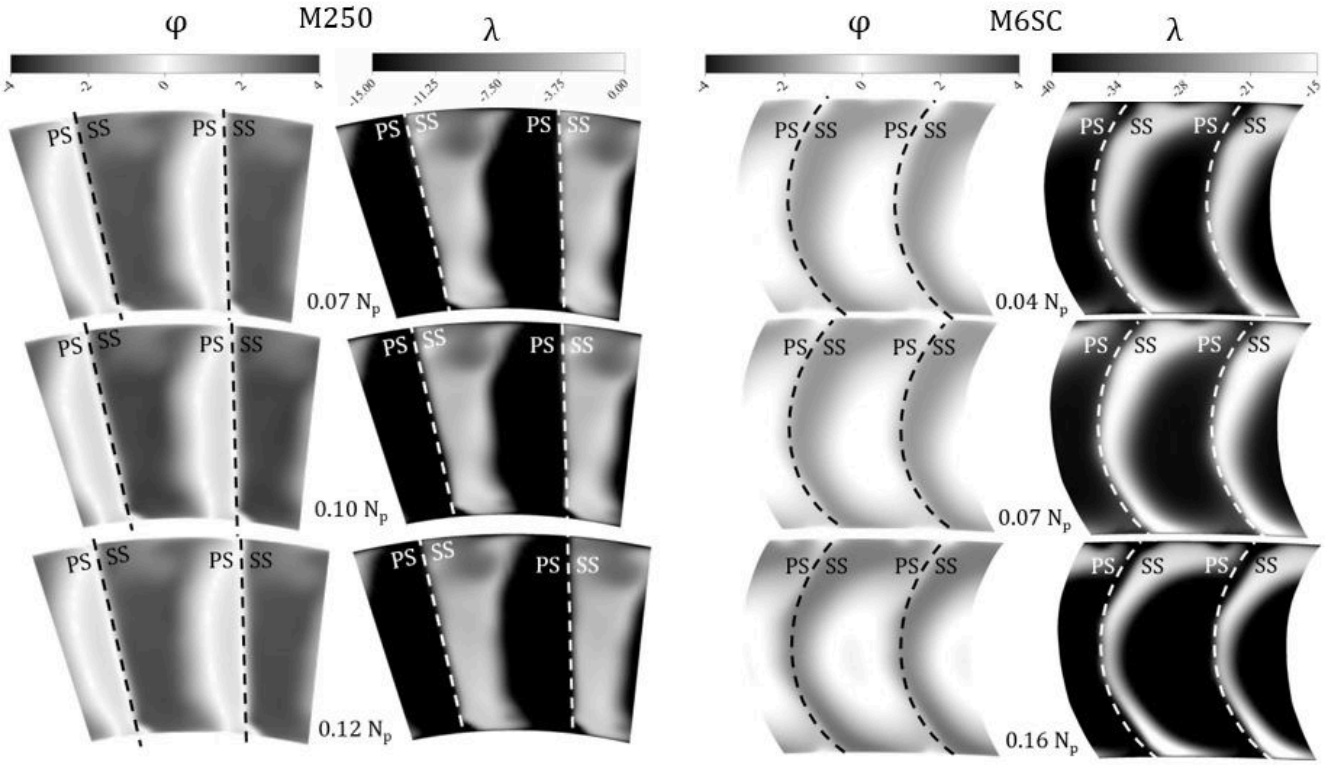

Fig. 20- Flow coefficient and pressure rise coefficient contours downstream of the OGV for the M250 and M6SC.

In all cases similar flow-fields result, with distinct areas of high pressure loss and low flow on the blading pressure side. The 0.16 Np case for the M6SC presents a slightly different flow-field to the rest, and this can be explained due to its proximity to the choking point, as the flow Mach number approaches 0.9. The similarity in flow-fields can only be considered for cases far from the choking condition, where compressibility effects are not a major factor. Nevertheless, the flow-field of the 0.16 Np M6SC case is still qualitatively comparable to the other two, and with the same magnitude loss and flow in terms of non-dimensional parameters.

4. Conclusion

A sub-idle compressor rig has been built to obtain locked rotor and windmill characteristics using an M250 6-stage axial compressor. The experimental results have shown the linear windmill speed–mass flow relationship and this has been re-created using computational fluid dynamics. The torque-free windmilling speed is predicted using a simple method to adjust the compressor mass flow until the torque is zeroed. Numerical and experimental results show the expected linear trend in windmill mass-flow versus speed and work distributions extracted from numerical results indicate that compressor loading is identical for all stages at different windmilling mass-flows. The axial work distributions at windmill show that the rear stages of multi-stage compressors operate like a turbine, extracting work from the flow in order to rotate and compress the air in the front stages. The stage immediately before this change, from work addition to extraction, incurs a pressure loss while still adding enthalpy to the flow, and is thus termed “stirrer”. For the two 6-stage compressor geometries studied numerically, stages 1-3 acted as compressors, stage 4 as a stirrer and stages 5 and 6 as a turbine. The majority of the pressure loss is due to the high-negative incidence flow present in the last stator, or OGV. Flow-field similarity has been shown to apply to compressor windmill discharge conditions at different windmilling speeds. These outcomes entail that a single windmill simulation can be used to characterize compressor performance for the entire windmilling regime.

The frozen rotor and mixing plane approaches have been compared for both the locked rotor and windmill cases. While a frozen-rotor approach has been used in the locked rotor scale to account for unequal pitches, the mixing plane approach has been deemed appropriate to model torque-free windmill cases. Pressure ratio is seen to be well matched against experiment for both the locked rotor and windmill cases. The accuracy of the steady state torque calculation is more modest when compared to experiment, while limited unsteady runs have shown that flow-field unsteadiness and RANS model deficiencies is likely to be the cause. The calculation of the windmill signature (the relationship between mass flow and torque-free windmill speed) by the CFD model is seen to match properly against experiment. The results presented in this work indicate that limited RANS simulations can be employed to estimate performance parameters at sub-idle in order to generate a map down to zero speed, while more detailed scale-resolving simulations would be needed to accurately predict the variations in locked-rotor torque due to unsteady vortex shedding.

Acknowledgements

The authors would like to thank Rolls-Royce plc for supporting this work and allowing its publication. This work has been co-founded by Innovate UK. Special thanks are due to Richard J. Tunstall of Rolls-Royce plc for his collaboration.

REFERENCES

[1] Agrawal, R. K., and M. Yunis. (1982). A generalized mathematical model to estimate gas turbine starting characteristics. Transactions of the ASME 104, pp. 194-201.

[2] ANSYS, Inc. (2016), Ansys CFX-Solver Theory Guide

[3] EASA (2015). Certification memorandum: turbine engine relighting in flight. Pub. L. No. CS-E 910, 1

[4] Erdos, J. I., Alzner, E., McNally, W., (1977). Numerical Solution of Periodic Transonic Flow through a Fan Stage. AIAA Journal, Vol. 15, No. 11 , pp. 1559-1568.

[5] Farokhi, S. (2014), Aircraft Propulsion, 2nd edition. John Wiley & Sons.

[6] Ferrer-Vidal, L.E., Pachidis, V., Tunstall, R. (2018). An enhanced compressor sub-idle map generation method. Proceedings of GPPS Forum 18. Zurich, Switzerland.

[7] Gaudet, S. R., & Gauthier, J. E. D. (2007). A simple sub-idle component map extrapolation method. ASME Turbo Expo 2007: Power for Land, Sea, and Air. Montreal, Canada. doi:10.1115/GT2007-27193

[8] Ghenaiet, A., Khalfallah, S. (2019), CFD based criteria of stall onset in centrifugal compressors, Aerospace Science and Technology, ISSN 1270-9638

[9] Howard, J. (2007), Sub-idle modelling of gas turbines; altitude Relight and windmilling. PhD Thesis, Cranfield University

[10] Hu, J., Li, Q., Pan, T., Gong, Y. (2019), Numerical investigations on stator hub initiated stall in a single-stage transonic axial compressor,Aerospace Science and Technology, Volume 80, Pages 144-155, ISSN 1270-9638

[11] Iglesias Perez, A. (2018), Scale-resolving simulations of compressor blading at negative incidences. Master's Thesis, Cranfield University

[12] Illana, E., Grech, N., Zachos, P. K., & Pachidis, V. (2013). Axial compressor aerodynamics under sub-idle conditions. ASME Turbo Expo 2013: Power for Land, Sea, and Air. San Antonio, Texas.

[13] Jones, G., Pilidis, P., and Curnock, B. (2001). Compressor characteristics in gas turbine performance modelling. ASME. Turbo Expo 2001: Power for Land, Sea, and Air. New Orleans, Louisiana

[14] Kim, S., Kim, K., Son, C., (2019) Three-dimensional unsteady simulation of a multistage axial compressor with labyrinth seals and its effects on overall performance and flow characteristics, Aerospace Science and Technology, Volume 86, Pages 683-693, ISSN 1270-9638

[15] Kurzke, J. (1996). How to get component maps for aircraft gas turbine performance calculations. International Gas Turbine and Aeroengine Congress and Exhibition (pp. 1–7)

[16] Leggett, J., Priebe, S., Shabbir, A., Michelassi, V., Sandberg, R.D. and Richardson, E. (2018) Loss prediction in an axial compressor cascade at off-design incidences with free stream disturbances using large Eddy simulation. Journal of Turbomachinery, 1-13. (doi:10.1115/1.4039807).

[17] Menter, F.R. (1994), Two-equation eddy-viscosity turbulence models for engineering applications, AIAA Journal, Vol. 32, No. 8, pp. 1598-1605

[18] Menter, F.R. (2015), Best practice: scale-resolving simulations in ANSYS CFD. ANSYS Inc.

[19] Riegler, C., Bauer, M., and Kurzke, J. (2001). Some aspects of modeling compressor behavior in gas turbine performance calculations. ASME Journal of Turbomachinery

[20] Righi, M., Pachidis, V., Könözsy, L., Pawsey, L. (2018), Three-dimensional through-flow modelling of axial flow compressor rotating stall and surge, Aerospace Science and Technology, Volume 78, Pages 271-279, ISSN 1270-9638

[21] Roache, P.J. (1994). Perspective: a method for uniform reporting of grid refinement studies. Journal of Fluids Engineering, Vol. 116

[22] Shou, Z.Q. (1981), Calculation of windmilling characteristics for turbojet engines. ASME Journal of Engineering for Power, Vol 103

[23] Spalart, P.R., Venkatakrishnan, V., (2016), On the role and challenges of CFD in the aerospace industry. The Aeronautical Journal, Vol 123 No 1223

[24] Pawsey, L., Rajendran, D.J., Pachidis, V. (2018), Characterisation of turbine behaviour for an engine overspeed prediction model. Aerospace Science and Technology, Volume 73, Pages 10-18, ISSN 1270-9638

[25] Prasad D. (2018), Aerodynamic similarity principles and scaling laws for windmilling fans. ASME. Turbo Expo: Power for Land, Sea, and Air, Volume 2A: Turbomachinery

[26] Walsh, P. and Fletcher, P. (2004). Gas Turbine Performance, (2nd ed). Oxford, UK: Blackwell Science

[27] Wilcox, D. C. (1993). Turbulence modeling for CFD. La Cañada, CA: DCW Industries, Inc.

[28] Zachos, P. K., Aslanidou, I., Pachidis, V., and Singh, R. (2011). A sub-idle compressor characteristic generation method with enhanced physical background. ASME Journal of Engineering for Gas Turbines and Power 133, doi: 10.1115/1.4002820

[29] Zachos, P. K. (2013). Modelling and analysis of turbofan engines under windmilling conditions. ASME Journal of Propulsion and Power, 29(4), 882–890., doi:10.2514/1.B34729

Characterization of axial compressor performance at locked rotor and torque-free windmill conditions

Ferrer-Vidal, Luis E.

2020-04-28

Ferrer-Vidal LE, Iglesias-Perez A, Pachidis V. (2020) Characterization of axial compressor performance at locked rotor and torque-free windmill conditions. Aerospace Science and Technology, Volume 101, June 2020, Article number 105846

https://doi.org/10.1016/j.ast.2020.105846